Journal of Modern Optics
Publication details, including instructions for authors and subscription information:
http://www.informaworld.com/smpp/title~content=t713191304

Inverse scattering for near-field scanning optical microscopy with broadband illumination

Brynmor J. Davis[a]; Jin Sun[b]; John C. Schotland[c]; P. Scott Carney[ab]
[a] The Beckman Institute for Advanced Science and Technology, University of Illinois, Urbana, Illinois 61801, USA [b] Department of Electrical and Computer Engineering, University of Illinois, Urbana, Illinois 61801, USA [c] Department of Bioengineering, University of Pennsylvania, Philadelphia, Pennsylvania, USA

First published on: 20 April 2010

To cite this Article Davis, Brynmor J. , Sun, Jin , Schotland, John C. and Scott Carney, P.(2010) 'Inverse scattering for near-field scanning optical microscopy with broadband illumination', Journal of Modern Optics,, First published on: 20 April 2010 (iFirst)
To link to this Article: DOI: 10.1080/09500341003698655
URL: http://dx.doi.org/10.1080/09500341003698655

Journal of Modern Optics
2010, 1–7, iFirst

Taylor & Francis
Taylor & Francis Group

Inverse scattering for near-field scanning optical microscopy with broadband illumination

Brynmor J. Davis[a], Jin Sun[b], John C. Schotland[c] and P. Scott Carney[a,b]*

[a]*The Beckman Institute for Advanced Science and Technology, University of Illinois, Urbana, Illinois 61801, USA;* [b]*Department of Electrical and Computer Engineering, University of Illinois, Urbana, Illinois 61801, USA;* [c]*Department of Bioengineering, University of Pennsylvania, Philadelphia, Pennsylvania, USA*

(*Received 22 October 2009; final version received 9 February 2010*)

The linear inverse problem for near-field optical microscopy is solved for a broadband scanning modality. Pseudo-inverse formulae are derived and illustrated with numerical simulations.

Keywords: near-field; tomography; microscopy; spectral; scanning probe; inverse problem

1. Introduction

The resolution of far-field optical imaging systems is subject to the diffraction limit [1]. To overcome this limit and infer structure at subwavelength scales, near-field techniques can be employed [2–8]. While near-field instruments produce data sensitive to subwavelength-scale sample variations, it is not necessarily obvious how the data relate to the physical properties of the sample [9,10]. In the last decade, there has been significant progress both in the modeling of near-field imaging systems and in the subsequent interpretation of the data collected, see e.g. [11]. In addition to allowing a quantitative understanding of the data collected by standard instruments, the modeling of near-field systems enables the application of computed imaging techniques [12]. That is, new near-field modalities with multiplex data-to-sample relations can be paired with numerical processing to infer sample structure, see e.g. [13–15]. The raw data need not provide an obvious representation of the spatial object structure.

Traditional near-field scanning optical microscopy (NSOM) systems collect data in two dimensions using probe scanning. To image a three-dimensional sample it is necessary to acquire additional data which, in near-field scanning optical tomography (NSOT), are then incorporated into the image using computed imaging techniques. For example, a microwave near-field tomography system has been demonstrated where additional data are acquired by scanning the sample using probes of different sizes [16]. Alternatively, additional near-field data may be collected using multiple observation angles or scan-heights [13,17–21].

In this work, a spectral NSOT modality is proposed. Rather than using multiple observation angles or multiple probes, it is proposed to collect data in a third dimension using the spectral degree of freedom. The approach of constructing an image in N spatial dimensions by collecting data in $(N-1)$ spatial dimensions and a spectral dimension has found application in techniques such as optical coherence tomography [22] and synthetic aperture radar [23]. The recent demonstration of an interferometric, spectral near-field system [24] suggests that this approach may also find success in NSOT. Multiple images corresponding to different wavelengths can be collected from each probe scan and are therefore inherently coregistered.

Broadband NSOT theory is developed below for two cases: a simplified model that provides a framework to understand. First, a scalar model with a simple source and background configuration is considered. Specifically, a point source is scanned above a perturbative sample. The sample is suspended in free-space for simplicity. Second, a more involved model is developed and proceeds along the same lines as the first. The field is taken to be a vector electromagnetic field in a background that includes a substrate. Following the monochromatic treatment given in [17], an instrument model is developed, an inversion formula based on the singular value

*Corresponding author. Email: carney@illinois.edu

ISSN 0950–0340 print/ISSN 1362–3044 online

DOI: 10.1080/09500341003698655
http://www.informaworld.com

decomposition (SVD) is derived, and simulations are used to determine the expected system performance.

2. Scalar forward problem

The first system considered is illustrated in Figure 1. The NSOT probe is assumed to behave as a point source illuminating the sample. The resulting scattered light is then collected coherently as a function of angle and/or wavelength depending on the NSOT modality considered. Using the first Born approximation (i.e. single scattering) the scattered field can then be expressed as

$$U(\boldsymbol{r}, \boldsymbol{r}_{\mathrm{d}}, k) = \int \mathrm{d}^3 r' G(\boldsymbol{r}, \boldsymbol{r}', k) G(\boldsymbol{r}', \boldsymbol{r}_{\mathrm{d}}, k) V(\boldsymbol{r}'), \tag{1}$$

where $\boldsymbol{r}$ is the position of the probe, $\boldsymbol{r}'$ is a dummy variable describing the scattering position within the sample, $\boldsymbol{r}_{\mathrm{d}}$ is the detector position, k is the wavenumber and the Green function is

$$G(\boldsymbol{r}, \boldsymbol{r}', k) = \exp(\mathrm{i}k|\boldsymbol{r}' - \boldsymbol{r}|)/|\boldsymbol{r}' - \boldsymbol{r}|. \tag{2}$$

Equation (1) describes light originating from a point source at $\boldsymbol{r}$, scattering from all sample positions $\boldsymbol{r}'$ and propagating to $\boldsymbol{r}_{\mathrm{d}}$. Here the NSOT system is described in illumination mode but the theory may be applied to detection mode by considering a source at $\boldsymbol{r}_{\mathrm{d}}$ and a point detector at $\boldsymbol{r}$. It is also implicit that the probe does not strongly interact with the sample – an approximation investigated in [20].

The second Green function in Equation (1) is asymptotically

$$G(\boldsymbol{r}', \boldsymbol{r}_{\mathrm{d}}, k) \sim \exp(-\mathrm{i}\boldsymbol{k} \cdot \boldsymbol{r}') \exp(\mathrm{i}kr_{\mathrm{d}})/r_{\mathrm{d}}, \tag{3}$$

since $\boldsymbol{r}_{\mathrm{d}}$ is in the far-field. Note that k and $\boldsymbol{r}_{\mathrm{d}}$ determine the detection wavevector $\boldsymbol{k}$ and that this approximation assumes $\boldsymbol{r}'$ is near the origin. Collecting the angular and spectral dependence of U in $\boldsymbol{k}$ and dropping dependence on r_{d} (the constant distance to a detection hemisphere) gives

$$U(\boldsymbol{r}, \boldsymbol{k}) = \int \mathrm{d}^3 r' G(\boldsymbol{r}, \boldsymbol{r}', k) \exp(-\mathrm{i}\boldsymbol{k} \cdot \boldsymbol{r}') V(\boldsymbol{r}'). \tag{4}$$

It is now convenient to express the remaining Green function using the Weyl representation [25]

$$G(\boldsymbol{r}, \boldsymbol{r}', k) = \frac{\mathrm{i}}{2\pi} \int \frac{\mathrm{d}^2 q}{k_z(\boldsymbol{q}, k)} \exp[\mathrm{i}\boldsymbol{q} \cdot (\boldsymbol{\rho} - \boldsymbol{\rho}') + \mathrm{i}k_z(\boldsymbol{q}, k)|z - z'|], \tag{5}$$

where $\boldsymbol{r} = (\boldsymbol{\rho}, z)$ and $k_z(\boldsymbol{q}, k) = (k^2 - q^2)^{1/2}$ (the principal branch is used to evaluate this square root).

It is assumed that the probe-scan plane is fixed above the sample and is set to $z = 0$. The definition $\boldsymbol{Q}(\boldsymbol{q}, k) = [\boldsymbol{q}, k_z(\boldsymbol{q}, k)]$ is used so that the data are written as

$$U(\boldsymbol{\rho}, \boldsymbol{k}) = \frac{\mathrm{i}}{2\pi} \int \frac{\mathrm{d}^2 q \exp(\mathrm{i}\boldsymbol{q} \cdot \boldsymbol{\rho})}{k_z(\boldsymbol{q}, k)} \int \mathrm{d}^3 r' \exp\{-\mathrm{i}[\boldsymbol{k} + \boldsymbol{Q}(\boldsymbol{q}, k)] \cdot \boldsymbol{r}'\} V(\boldsymbol{r}'). \tag{6}$$

Taking the Fourier transform with respect to the scan dimensions $\boldsymbol{\rho}$,

$$\tilde{U}(\boldsymbol{q}, \boldsymbol{k}) = \frac{2\pi\mathrm{i}}{k_z(\boldsymbol{q}, k)} \int \mathrm{d}^3 r' \exp\{-\mathrm{i}[\boldsymbol{k} + \boldsymbol{Q}(\boldsymbol{q}, k)] \cdot \boldsymbol{r}'\} V(\boldsymbol{r}'), \tag{7}$$

where $\tilde{}$ represents a transverse Fourier transform. The transverse Fourier transform contained in the remaining integral can also be evaluated by defining $\tilde{V}$, the two-dimensional transverse Fourier transform of V. The observation model now simplifies to a one-dimensional integral equation,

$$\tilde{U}(\boldsymbol{q}, \boldsymbol{k}) = \frac{2\pi\mathrm{i}}{k_z(\boldsymbol{q}, k)} \int \mathrm{d}z' \exp\{-\mathrm{i}[k_z(\boldsymbol{k}_{\parallel}, k) + k_z(\boldsymbol{q}, k)]z'\} \tilde{V}(\boldsymbol{k}_{\parallel} + \boldsymbol{q}, z'), \tag{8}$$

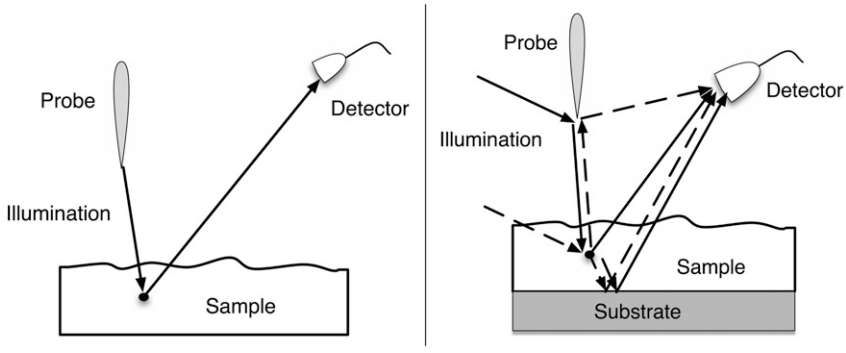

Figure 1. The scalar model considered first is illustrated on the left. The probe is the source of illumination and the sample is in free-space (so there is no substrate to produce reflections). The vector model considered second is illustrated on the right. The probe–sample system is illuminated. The illumination is scattered from both the probe and the inhomogeneities in the sample. The scattered field is reflected from a supporting substrate.

where $\boldsymbol{k}=[\boldsymbol{k}_\parallel, k_z(\boldsymbol{k}_\parallel, k)]$. This model applies to multi-angle and/or broadband NSOM. The dependence on both angle and wavelength is contained in $\boldsymbol{k}$.

The Fourier-domain model expressed in Equation (8) implicitly assumes an infinite and continuous scan range. A finite and discrete sampling grid approximates Equation (8), provided that the probe scanning step is sufficiently small to preclude aliasing and the scan range covers all significant signal.

3. Scalar inverse problem

While the model given in Equation (1) could be used in the design of an inversion process, Equation (8) is much more appealing as it is only a one-dimensional integral equation. The transverse component of the data collection is linear and shift-invariant and is therefore diagonalized in the Fourier-domain, reducing the dimensionality of the problem. Regarding the transverse Fourier-transform variables $\boldsymbol{q}$ as parameters, the model can be rewritten,

$$\begin{aligned}\tilde{\mathcal{U}}_{\boldsymbol{q}}(\boldsymbol{k}) &= \left[A_{\boldsymbol{q}}\tilde{V}_{\boldsymbol{q}}\right](\boldsymbol{k}) \\ &= \int \mathrm{d}z \exp\{-\mathrm{i}[k_z(\boldsymbol{k}_\parallel, k) + k_z(\boldsymbol{q}-\boldsymbol{k}_\parallel, k)]z\}\tilde{V}_{\boldsymbol{q}}(z),\end{aligned} \tag{9}$$

where $\tilde{\mathcal{U}}_{\boldsymbol{q}}(\boldsymbol{k}) = k_z(\boldsymbol{q}-\boldsymbol{k}_\parallel, k)\tilde{U}(\boldsymbol{q}-\boldsymbol{k}_\parallel, \boldsymbol{k})/(2\pi\mathrm{i})$. The operator kernel is

$$A_{\boldsymbol{q}}(\boldsymbol{k}, z) = \exp\{\mathrm{i}[k_z^*(\boldsymbol{k}_\parallel, k) + k_z^*(\boldsymbol{q}-\boldsymbol{k}_\parallel, k)]z\}, \tag{10}$$

with $[A_{\boldsymbol{q}}u](\boldsymbol{k}) = \langle A_{\boldsymbol{q}}\ (\boldsymbol{k}, z),\ u(z)\rangle_z$, and angle brackets denoting an inner-product. In z space, $\langle s(z), u(z)\rangle_z = \int \mathrm{d}z\, s^*(z)u(z)$. The adjoint operator is $A_{\boldsymbol{q}}^\dagger$, with $[A_{\boldsymbol{q}}^\dagger w](z) = \langle A_{\boldsymbol{q}}^*(\boldsymbol{k}, z), w(\boldsymbol{k})\rangle_{\boldsymbol{k}}$ and the $\boldsymbol{k}$-space inner-product being $\langle v(\boldsymbol{k}), w(\boldsymbol{k})\rangle_{\boldsymbol{k}} = \sum_{\boldsymbol{k}} v^*(\boldsymbol{k})w(\boldsymbol{k})$. The operator $A_{\boldsymbol{q}}$ maps a continuous function on z to data collected on a discrete set $\mathcal{K}$ of $\boldsymbol{k}$ vectors. The SVD analysis of such semi-discrete systems is standard [26] and will be used to invert the mapping from z to $\mathcal{K}$.

The Gram matrix for $A_{\boldsymbol{q}}$ is

$$\begin{aligned}M_{\boldsymbol{q}}(\boldsymbol{k}, \boldsymbol{k}') &= \langle A_{\boldsymbol{q}}(\boldsymbol{k}, z), A_{\boldsymbol{q}}(\boldsymbol{k}', z)\rangle_z, \\ &= \begin{cases} \left.\dfrac{\exp[-\mathrm{i}\mathcal{Q}(\boldsymbol{q}, \boldsymbol{k}, \boldsymbol{k}')z]}{-\mathrm{i}\mathcal{Q}(\boldsymbol{q}, \boldsymbol{k}, \boldsymbol{k}')}\right|_{z_{\min}}^{z_{\max}}, & \mathcal{Q}(\boldsymbol{q}, \boldsymbol{k}, \boldsymbol{k}') \neq 0, \\ z_{\max} - z_{\min}, & \mathcal{Q}(\boldsymbol{q}, \boldsymbol{k}, \boldsymbol{k}') = 0, \end{cases}\end{aligned} \tag{11}$$

where $\boldsymbol{k}$ and $\boldsymbol{k}'$ index the rows and columns, respectively,

$$\begin{aligned}\mathcal{Q}(\boldsymbol{q}, \boldsymbol{k}, \boldsymbol{k}') &= k_z(\boldsymbol{k}_\parallel, k) - k_z^*(\boldsymbol{k}_\parallel', k') + k_z(\boldsymbol{q}-\boldsymbol{k}_\parallel, k) \\ &\quad - k_z^*(\boldsymbol{q}-\boldsymbol{k}_\parallel', k'),\end{aligned} \tag{12}$$

and $z_{\min}$ and $z_{\max}$ giving the longitudinal boundaries of the sample. Matrix multiplication by $M_{\boldsymbol{q}}$ is a mapping from $\mathcal{K}$ to $\mathcal{K}$ and represents the normal operator for this system. Note that the Gram matrix is Hermitian and nonnegative definite.

The real nonnegative eigenvalues of $M_{\boldsymbol{q}}$ and the corresponding eigenvectors are found numerically. The ℓth eigenvector $c_{\boldsymbol{q}}^\ell(\boldsymbol{k})$ (where the measurement wavevector $\boldsymbol{k}$ indexes the vector element) is the ℓth left-singular vector of $A_{\boldsymbol{q}}$, and the square root of the ℓth eigenvalue of $M_{\boldsymbol{q}}$ is the singular value $\sigma_{\boldsymbol{q}}^\ell$. The ℓth right singular vector can then be calculated as,

$$\psi_{\boldsymbol{q}}^\ell(z) = \left[A_{\boldsymbol{q}}^\dagger c_{\boldsymbol{q}}^\ell\right](z) = \langle A_{\boldsymbol{q}}^*(\boldsymbol{k}, z), c_{\boldsymbol{q}}^\ell(\boldsymbol{k})\rangle_{\boldsymbol{k}}. \tag{13}$$

This defines the SVD, so $\tilde{\mathcal{U}}_{\boldsymbol{q}}(\boldsymbol{k})$ can be expressed as

$$\left[A_{\boldsymbol{q}}\tilde{V}_{\boldsymbol{q}}\right](\boldsymbol{k}) = \sum_{\ell=1}^{N} \sigma_{\boldsymbol{q}}^\ell c_{\boldsymbol{q}}^\ell(\boldsymbol{k})\langle\psi_{\boldsymbol{q}}^\ell(z), \tilde{V}_{\boldsymbol{q}}(z)\rangle_z, \tag{14}$$

where N is the number of elements in $\mathcal{K}$.

The preprocessed data $\tilde{\mathcal{U}}_{\boldsymbol{q}}$ can then be used in the inversion of Equation (9). The truncated singular value decomposition (TSVD) is employed to find $\tilde{V}_{\boldsymbol{q}}^+(z)$, an estimate of the sample in $\boldsymbol{q}$–z space. The TSVD is used to provide stability to noise and is expressed as

$$\tilde{V}_{\boldsymbol{q}}^+(z) = \sum_{\ell=1}^{N^+} \frac{1}{\sigma_{\boldsymbol{q}}^\ell}\psi_{\boldsymbol{q}}^\ell(z)\langle c_{\boldsymbol{q}}^\ell(\boldsymbol{k}), \tilde{\mathcal{U}}_{\boldsymbol{q}}(\boldsymbol{k})\rangle_{\boldsymbol{k}}, \tag{15}$$

where N^+ is the number of singular components included in the reconstruction. The regularization of the inverse problem is controlled by N^+ – a greater N^+ gives better reconstruction fidelity while a lesser N^+ reduces sensitivity to measurement noise.

4. Vector forward problem

We turn our attention to a model more applicable to optical near-field microscopy, but superficially more complicated. In this section, a vector field is considered. The tip serves as a scatterer of illuminating light rather than a primary source. The realistic presence of a supporting substrate is included in the incident field and the Green tensor. The data are assumed measured on a discrete grid. Despite rather longer expressions, the structure of the problem remains largely the same. The illumination, scattering by the tip then the sample, scattering by the sample then the tip, reflections from the substrate and subsequent detection are illustrated in Figure 1.

A weakly scattering sample, described by the dielectric susceptibility $\eta(\boldsymbol{r})$ (rather than the scattering potential V for scalar fields), is placed in vacuum above a half-space with a uniform index of refraction n. The interface is assumed to coincide with the $z=0$ plane.

An apertureless tip with an effective polarizability $\boldsymbol{\alpha}_e$ [20] is scanned over the sample while the system is illuminated by an incident plane wave $\boldsymbol{E}^{\mathrm{i}}$, with free-space wave vector $\boldsymbol{k}_{\mathrm{d}} = -[\boldsymbol{q}_{\mathrm{d}},\ k_z(\boldsymbol{k}_{\mathrm{d}},\ k)]$, and polarization $\boldsymbol{p}$, given by

$$\boldsymbol{E}^{\mathrm{i}}(\boldsymbol{r}, \boldsymbol{k}_{\mathrm{d}}) = \left(\boldsymbol{I} + \mathcal{R}(-\boldsymbol{q}_{\mathrm{d}}, k)\exp[2\mathrm{i}k_z(\boldsymbol{q}_{\mathrm{d}}, k)z]\right) \exp[\mathrm{i}\boldsymbol{q}_{\mathrm{d}} \cdot \boldsymbol{\rho} - \mathrm{i}k_z(\boldsymbol{q}_{\mathrm{d}}, k)z]\boldsymbol{p}, \tag{16}$$

where $\mathcal{R}$ is the reflection tensor at the half-space interface [20].

The detector is assumed to be placed to collect the back-reflection. That is the position of the detector is given by $\boldsymbol{r}_{\mathrm{d}} = (\boldsymbol{\rho}_{\mathrm{d}}, z_{\mathrm{d}})$, a vector parallel to $\boldsymbol{k}_{\mathrm{d}}$. At the detector, the same polarization as was incident, $\boldsymbol{p}$ is assumed to be measured. The first Born approximation (linear in the sample susceptibility) is given by [20]

$$E_{\mathrm{s}} = \boldsymbol{p} \cdot [\boldsymbol{TS} + \boldsymbol{ST}] \cdot \boldsymbol{E}^{\mathrm{i}}, \tag{17}$$

where $\boldsymbol{T}$ and $\boldsymbol{S}$ represent integral operators mapping a field incident on the tip or the sample to the respective scattered field. They are given by

$$[\boldsymbol{S} \cdot \boldsymbol{E}](\boldsymbol{r}) = k^2 \int \mathrm{d}^3 r'\, \boldsymbol{G}(\boldsymbol{r}, \boldsymbol{r}', k)\eta(\boldsymbol{r}')\boldsymbol{E}(\boldsymbol{r}'), \tag{18}$$

and

$$[\boldsymbol{T} \cdot \boldsymbol{E}](\boldsymbol{r}) = k^2 \int \mathrm{d}^3 r'\, \boldsymbol{G}(\boldsymbol{r}, \boldsymbol{r}', k)\boldsymbol{\alpha}_e \delta(\boldsymbol{r}' - \boldsymbol{r}_{\mathrm{t}})\boldsymbol{E}(\boldsymbol{r}'), \tag{19}$$

where $\boldsymbol{r}_{\mathrm{t}} = (\boldsymbol{\rho}_{\mathrm{t}}, z_{\mathrm{t}})$ is the position of the tip and $\boldsymbol{G}$ is the half-space Green tensor. It may be noted that while the scattering from the tip is exactly described by $\boldsymbol{T}$, the scattering from the sample, described by $\boldsymbol{S}$, is of first-Born type [20].

The Green tensor may be expressed in the plane wave decomposition [20]

$$\boldsymbol{G}(\boldsymbol{r}, \boldsymbol{r}', k) = \frac{\mathrm{i}}{2\pi} \int \mathrm{d}^2 q\, \boldsymbol{g}(z, z', k; \boldsymbol{q}) \exp[\mathrm{i}\boldsymbol{q} \cdot (\boldsymbol{\rho} - \boldsymbol{\rho}')], \tag{20}$$

where $\boldsymbol{g}(z, z'; \boldsymbol{q})$, the plane wave component, is given by

$$\boldsymbol{g}(z, z', k; \boldsymbol{q}) = \frac{1}{k_z(\boldsymbol{q}, k)} \begin{cases} \left[\mathcal{D}(\boldsymbol{q})\exp[\mathrm{i}k_z(\boldsymbol{q}, \boldsymbol{k})(z - z')] \right. \\ \quad \left. + \mathcal{R}(\boldsymbol{q})\exp[\mathrm{i}k_z(\boldsymbol{q}, \boldsymbol{k})(z + z')]\right], & 0 \le z' \le z, \\ \left[\tilde{\mathcal{D}}(\boldsymbol{q})\exp[\mathrm{i}k_z(\boldsymbol{q}, k)(z' - z)] \right. \\ \quad \left. + \mathcal{R}(\boldsymbol{q}, k)\exp[\mathrm{i}k_z(\boldsymbol{q})(z' + z)]\right], & 0 \le z < z', \end{cases} \tag{21}$$

where dependence on the wave number k of the polarization tensors $\mathcal{D}(\boldsymbol{q})$ and $\tilde{\mathcal{D}}(\boldsymbol{q})$, the reflection tensor $\mathcal{R}(\boldsymbol{q})$ and the transmission tensors $\mathcal{T}(\boldsymbol{q})$ and $\mathcal{T}'(\boldsymbol{q})$, which were given in [20], is understood. The Green tensor has the asymptotic form

$$\boldsymbol{G}(\boldsymbol{r}_{\mathrm{d}}, \boldsymbol{r}', k_{\mathrm{d}}) = \frac{\exp(\mathrm{i}kr_{\mathrm{d}})}{r_{\mathrm{d}}} \exp(-\mathrm{i}\boldsymbol{k}_{\mathrm{d}} \cdot \boldsymbol{r}') \times \left[\mathcal{D}(\boldsymbol{q}_{\mathrm{d}}) + \mathcal{R}(\boldsymbol{q}_{\mathrm{d}})\exp[2\mathrm{i}k_z(\boldsymbol{q}_{\mathrm{d}}, k)z']\right] \tag{22}$$

with the observation point $\boldsymbol{r}_{\mathrm{d}}$ in the far field in the upper half space and the source point $\boldsymbol{r}'$ near the origin in the upper half space. Making use of Equations (18), (19), (22), it is seen that the scattered field given by Equation (17) can be represented by the scattering amplitude $A = A_{TS} + A_{ST}$, i.e.

$$E_{\mathrm{s}}(\boldsymbol{r}_{\mathrm{d}}, \boldsymbol{r}_{\mathrm{t}}, \boldsymbol{k}_{\mathrm{d}}) = \frac{\exp(\mathrm{i}kr_{\mathrm{d}})}{r_{\mathrm{d}}} A(\boldsymbol{r}_{\mathrm{t}}, \boldsymbol{k}_{\mathrm{d}}), \tag{23}$$

where

$$A_{TS}(\boldsymbol{r}_{\mathrm{t}}, \boldsymbol{k}_{\mathrm{d}}) = k^4 \int \mathrm{d}^3 r' \exp[-\mathrm{i}\boldsymbol{k}_{\mathrm{d}} \cdot (\boldsymbol{r}_{\mathrm{t}} + \boldsymbol{r}')]\boldsymbol{p} \cdot \left[\mathcal{D}(\boldsymbol{q}_{\mathrm{d}}) + \mathcal{R}(\boldsymbol{q}_{\mathrm{d}})\exp[2\mathrm{i}k_z(\boldsymbol{q}_{\mathrm{d}}, k)z_{\mathrm{t}}]\right]\boldsymbol{\alpha}_e \boldsymbol{G}(\boldsymbol{r}_{\mathrm{t}}, \boldsymbol{r}', k) \times [\boldsymbol{I} + \mathcal{R}(-\boldsymbol{q}_{\mathrm{d}})e^{2\mathrm{i}k_z(\boldsymbol{q}_{\mathrm{d}}, k)z'}]\boldsymbol{p}\,\eta(\boldsymbol{r}'), \tag{24}$$

$$A_{ST}(\boldsymbol{r}_{\mathrm{t}}, \boldsymbol{k}_{\mathrm{d}}) = k^4 \int \mathrm{d}^3 r' \exp[-\mathrm{i}\boldsymbol{k}_{\mathrm{d}} \cdot (\boldsymbol{r}' + \boldsymbol{r}_{\mathrm{t}})]\boldsymbol{p} \cdot \left[\mathcal{D}(\boldsymbol{q}_{\mathrm{d}}) + \mathcal{R}(\boldsymbol{q}_{\mathrm{d}})\exp[2\mathrm{i}k_z(\boldsymbol{q}_{\mathrm{d}}, k)z']\right]\boldsymbol{G}(\boldsymbol{r}', \boldsymbol{r}_{\mathrm{t}}, k)\boldsymbol{\alpha}_e \times \left[\boldsymbol{I} + \mathcal{R}(-\boldsymbol{q}_{\mathrm{d}})\exp[2\mathrm{i}k_z(\boldsymbol{q}_{\mathrm{d}}, k)z_{\mathrm{t}}]\right]\boldsymbol{p}\,\eta(\boldsymbol{r}'). \tag{25}$$

Note that $\boldsymbol{p}$ represents a certain TEM polarization in the propagation direction defined by $\boldsymbol{k}_{\mathrm{d}}$, and therefore lies in the invariant subspace of the polarization operator $\mathcal{D}(\boldsymbol{q}_{\mathrm{d}})$, which implies that $\boldsymbol{p} \cdot \mathcal{D}(\boldsymbol{q}_{\mathrm{d}}) = \boldsymbol{p}$. Assuming $\boldsymbol{\alpha}_e$ is a symmetric tensor, i.e. $\boldsymbol{\alpha}_e = \boldsymbol{\alpha}_e^{\mathrm{T}}$ where superscript 'T' represents matrix transpose, and considering that [20] $\mathcal{R}(-\boldsymbol{q}_{\mathrm{d}}) = \mathcal{R}^{\mathrm{T}}(\boldsymbol{q}_{\mathrm{d}})$ and $\boldsymbol{G}(\boldsymbol{r}', \boldsymbol{r}_{\mathrm{t}}, k) = \boldsymbol{G}^{\mathrm{T}}(\boldsymbol{r}_{\mathrm{t}}, \boldsymbol{r}', k)$, it may be seen that $A_{ST} = A_{TS}^{\mathrm{T}} = A_{TS}$ since A_{TS} is a scalar quantity. Hence, the scattered field may be represented by its amplitude $A(\boldsymbol{r}_{\mathrm{t}}, \boldsymbol{k}_{\mathrm{d}}) = 2A_{TS}(\boldsymbol{r}_{\mathrm{t}}, \boldsymbol{k}_{\mathrm{d}})$.

Following the procedures outlined above and in [20], we define the data function Φ as the lattice Fourier transform of $A(\boldsymbol{r}_{\mathrm{t}}, \boldsymbol{k}_{\mathrm{d}}) = 2A_{TS}(\boldsymbol{r}_{\mathrm{t}}, \boldsymbol{k}_{\mathrm{d}})$ with respect to $\boldsymbol{\rho}_{\mathrm{t}}$ with lattice spacing h,

$$\Phi(\boldsymbol{q}_{\mathrm{t}}, z_{\mathrm{t}}, \boldsymbol{k}_{\mathrm{d}}) = h^2 \sum_{\rho_{\mathrm{t}}} A(\boldsymbol{r}_{\mathrm{t}}, \boldsymbol{k}_{\mathrm{d}}) \exp(-\mathrm{i}\boldsymbol{q}_{\mathrm{t}} \cdot \boldsymbol{\rho}_{\mathrm{t}}), \tag{26}$$

where the sum over $\boldsymbol{\rho}_{\mathrm{t}}$ is carried out over all lattice vectors and $\boldsymbol{q}_{\mathrm{t}}$ belongs to the first Brillouin zone (FBZ) of the lattice. In this case FBZ $= [-\pi/h,\ \pi/h] \times [-\pi/h,\ \pi/h]$. By substituting Equation (24) into Equation (26) and making use of the plane wave representation of the Green tensor (20), and the identity

$$\sum_{\rho} \exp(\mathrm{i}\boldsymbol{q} \cdot \boldsymbol{\rho}) = \left(\frac{2\pi}{h}\right)^2 \sum_{\boldsymbol{q}''} \delta(\boldsymbol{q} - \boldsymbol{q}''), \tag{27}$$

where $\boldsymbol{q}''$ denotes a reciprocal lattice vector, the data function is expressed as

$$\Phi(\boldsymbol{q}_\mathrm{t}, z_\mathrm{t}, \boldsymbol{k}_\mathrm{d}) = k_z^{-1}(\boldsymbol{q}_\mathrm{d}+\boldsymbol{q}_\mathrm{t}, k)\int \mathrm{d}z'\, L(\boldsymbol{q}_\mathrm{t}, z_\mathrm{t}, \boldsymbol{k}_\mathrm{d}, z')\tilde{\eta}(2\boldsymbol{q}_\mathrm{d}+\boldsymbol{q}_\mathrm{t}, z'), \tag{28}$$

where $\tilde{\eta}(\boldsymbol{q}, z') = \int \mathrm{d}^2\rho'\, \eta(\boldsymbol{\rho}', z')\exp[-\mathrm{i}\boldsymbol{q}\cdot\boldsymbol{\rho}']$ is the lateral Fourier transform of the sample function η, assumed to be band-limited to the FBZ, and the kernel of integration L is given by

$$\begin{aligned} L(\boldsymbol{q}_\mathrm{t}, z_\mathrm{t}, \boldsymbol{k}_\mathrm{d}, z') = {} & 4\pi\mathrm{i}k^4 \exp\{\mathrm{i}[k_z(\boldsymbol{q}_\mathrm{d}+\boldsymbol{q}_\mathrm{t}, k) \\ & - k_z(\boldsymbol{q}_\mathrm{d}, k)]z_\mathrm{t}\}\boldsymbol{p}\cdot\big[\mathcal{D}(\boldsymbol{q}_\mathrm{d}) \\ & + \mathcal{R}(\boldsymbol{q}_\mathrm{d})\exp[2\mathrm{i}k_z(\boldsymbol{q}_\mathrm{d}, k)z_\mathrm{t}]\big] \\ & \times \boldsymbol{\alpha}_e\big[\mathcal{D}(\boldsymbol{q}_\mathrm{d}+\boldsymbol{q}_\mathrm{t})\exp[-\mathrm{i}k_z(\boldsymbol{q}_\mathrm{d}+\boldsymbol{q}_\mathrm{t}, k)z'] \\ & + \mathcal{R}(\boldsymbol{q}_\mathrm{d}+\boldsymbol{q}_\mathrm{t})\exp[\mathrm{i}k_z(\boldsymbol{q}_\mathrm{d}+\boldsymbol{q}_\mathrm{t}, k)z']\big] \\ & \times \big[\boldsymbol{I}\exp[-\mathrm{i}k_z(\boldsymbol{q}_\mathrm{d}, k)z'] + \mathcal{R}(-\boldsymbol{q}_\mathrm{d}) \\ & \times \exp[\mathrm{i}k_z(\boldsymbol{q}_\mathrm{d}, k)z']\big]\boldsymbol{p}. \end{aligned} \tag{29}$$

Equation (28) is the block-diagonalized forward integral equation, and is more suitable for a numerical inversion than Equations (24) and (25).

5. Vector inverse problem

The inversion of Equation (28) is very much similar to the procedure described above for the scalar case. Only key results are listed below.

By observation, the integral kernel L in Equation (29) contains a sum of terms like those appearing in the scalar case, cf. Equation (10). It may be written in the form of a separation of variables

$$L_{\boldsymbol{Q}}(\boldsymbol{k}_\mathrm{d}, z) = \sum_{j=1}^{4} C_{\boldsymbol{Q}}^{(j)}(\boldsymbol{k}_\mathrm{d})\exp\Big[-\mathrm{i}\lambda_{\boldsymbol{Q}}^{(j)}(\boldsymbol{k}_\mathrm{d})z\Big], \tag{30}$$

where subscript $\boldsymbol{Q}$ denotes collectively the parameters $(z_\mathrm{t}, 2\boldsymbol{q}_\mathrm{d}+\boldsymbol{q}_\mathrm{t})$, which are held constant during the reconstruction of one component of $\tilde{\eta}$, i.e. $\tilde{\eta}(2\boldsymbol{q}_\mathrm{d}+\boldsymbol{q}_\mathrm{t}, z) \equiv \tilde{\eta}_{\boldsymbol{Q}}(z)$. The coefficients $C_{\boldsymbol{Q}}^{(j)}$ and $\lambda_{\boldsymbol{Q}}^{(j)}$ are given by

$$\begin{aligned} & \left.\begin{aligned} C_{\boldsymbol{Q}}^{(1)}(\boldsymbol{k}_\mathrm{d}) &= \boldsymbol{p}\cdot\mathcal{D}(\boldsymbol{q}_\mathrm{d}+\boldsymbol{q}_\mathrm{t}) \\ C_{\boldsymbol{Q}}^{(2)}(\boldsymbol{k}_\mathrm{d}) &= \boldsymbol{p}\cdot\mathcal{R}(\boldsymbol{q}_\mathrm{d})\mathcal{D}(\boldsymbol{q}_\mathrm{d}+\boldsymbol{q}_\mathrm{t}) \\ C_{\boldsymbol{Q}}^{(3)}(\boldsymbol{k}_\mathrm{d}) &= \boldsymbol{p}\cdot\mathcal{R}(-\boldsymbol{q}_\mathrm{d}-\boldsymbol{q}_\mathrm{t}) \\ C_{\boldsymbol{Q}}^{(4)}(\boldsymbol{k}_\mathrm{d}) &= \boldsymbol{p}\cdot\mathcal{R}(\boldsymbol{q}_\mathrm{d})\mathcal{R}(-\boldsymbol{q}_\mathrm{d}-\boldsymbol{q}_\mathrm{t}) \end{aligned}\right\}\cdot 4\pi\mathrm{i}k^4\boldsymbol{\alpha}_e \\ & \times\Big[\boldsymbol{I}+\mathcal{R}(-\boldsymbol{q}_\mathrm{d})\exp[2\mathrm{i}k_z(\boldsymbol{q}_\mathrm{d}, k)z_\mathrm{t}]\Big]\boldsymbol{p} \\ & \times\exp\{\mathrm{i}[k_z(\boldsymbol{q}_\mathrm{d}+\boldsymbol{q}_\mathrm{t}, k) - k_z(\boldsymbol{q}_\mathrm{d}, k)]z_\mathrm{t}\} \end{aligned} \tag{31}$$

and

$$\begin{aligned} \lambda_{\boldsymbol{Q}}^{(1)}(\boldsymbol{k}_\mathrm{d}) &= k_z(\boldsymbol{q}_\mathrm{d}, k) + k_z(\boldsymbol{q}_\mathrm{d}+\boldsymbol{q}_\mathrm{t}, k), \\ \lambda_{\boldsymbol{Q}}^{(2)}(\boldsymbol{k}_\mathrm{d}) &= -k_z(\boldsymbol{q}_\mathrm{d}, k) + k_z(\boldsymbol{q}_\mathrm{d}+\boldsymbol{q}_\mathrm{t}, k), \\ \lambda_{\boldsymbol{Q}}^{(3)}(\boldsymbol{k}_\mathrm{d}) &= k_z(\boldsymbol{q}_\mathrm{d}, k) - k_z(\boldsymbol{q}_\mathrm{d}+\boldsymbol{q}_\mathrm{t}, k), \\ \lambda_{\boldsymbol{Q}}^{(4)}(\boldsymbol{k}_\mathrm{d}) &= -k_z(\boldsymbol{q}_\mathrm{d}, k) - k_z(\boldsymbol{q}_\mathrm{d}+\boldsymbol{q}_\mathrm{t}, k). \end{aligned} \tag{32}$$

The Gram matrix $M_{\boldsymbol{Q}}(\boldsymbol{k}_\mathrm{d}, \boldsymbol{k}_\mathrm{d}')$, cf. Equation (11), defined as

$$M_{\boldsymbol{q}}(\boldsymbol{k}_\mathrm{d}, \boldsymbol{k}_\mathrm{d}') = \int \mathrm{d}z L_{\boldsymbol{q}}(\boldsymbol{k}_\mathrm{d}, z)L_{\boldsymbol{Q}}^*(\boldsymbol{k}_\mathrm{d}', z), \tag{33}$$

where the integral is carried over an interval in which the sample function is supported, is found to be

$$M_{\boldsymbol{Q}}(\boldsymbol{k}_\mathrm{d}, \boldsymbol{k}_\mathrm{d}') = \sum_{j,l=1}^{4} C_{\boldsymbol{Q}}^{(j)}(\boldsymbol{k}_\mathrm{d})C_{\boldsymbol{Q}}^{(l)}(\boldsymbol{k}_\mathrm{d}')^* \times \frac{\exp\Big\{\mathrm{i}\Big[\lambda_{\boldsymbol{Q}}^{(l)}(\boldsymbol{k}_\mathrm{d}')^* - \lambda_{\boldsymbol{Q}}^{(j)}(\boldsymbol{k}_\mathrm{d})\Big]z_{\max}\Big\} - 1}{\mathrm{i}[\lambda_{\boldsymbol{Q}}^{(l)}(\boldsymbol{k}_\mathrm{d}')^* - \lambda_{\boldsymbol{Q}}^{(j)}(\boldsymbol{k}_\mathrm{d})]}, \tag{34}$$

where $z_{\max}$ is the maximum height of the sample, and the singularities at points, where the denominator is zero, are of removable type. A regularized solution is thus given by

$$\tilde{\eta}_{\boldsymbol{Q}}^{+}(z) = \sum_{\boldsymbol{k}_\mathrm{d}, \boldsymbol{k}_\mathrm{d}'} L_{\boldsymbol{Q}}^*(z, \boldsymbol{k}_\mathrm{d})M_{\boldsymbol{Q}}^{+}(\boldsymbol{k}_\mathrm{d}, \boldsymbol{k}_\mathrm{d}')\tilde{\Phi}_{\boldsymbol{Q}}(\boldsymbol{k}_\mathrm{d}'), \tag{35}$$

where $M_{\boldsymbol{Q}}^{+}$ is the regularized pseudo-inverse of the Gram matrix, and

$$\tilde{\Phi}_{\boldsymbol{Q}}(\boldsymbol{k}_\mathrm{d}') = k_z(\boldsymbol{q}_\mathrm{d}'+\boldsymbol{q}_\mathrm{t}, k)\Phi(\boldsymbol{q}_\mathrm{t}', z_\mathrm{t}, \boldsymbol{k}_\mathrm{d}') \tag{36}$$

is the preprocessed data. Regularization of the Gram matrix inversion may be trivially modified to achieve the same effects as regularizing inversion of the forward operator. The corresponding object reconstruction may be obtained through a two-dimensional inverse Fourier transform, usually realized by a fast Fourier transform (FFT) algorithm.

6. Simulations

The performance of the broadband NSOT systems is investigated using numerical simulations. Synthetic data are generated by defining a test sample $V(\boldsymbol{r})$ and evaluating Equation (1) for the modality considered. In this case the sample consists of four point scatterers at $(-3, 0, -0.15)\lambda$, $(-1.5, 0, -0.35)\lambda$, $(0, 0, -0.55)\lambda$ and $(1.5, 0, -0.75)\lambda$, where λ is a nominal wavelength. The first scatterer has a scattering potential 80% lower than the other scatterers in order to give a reconstruction

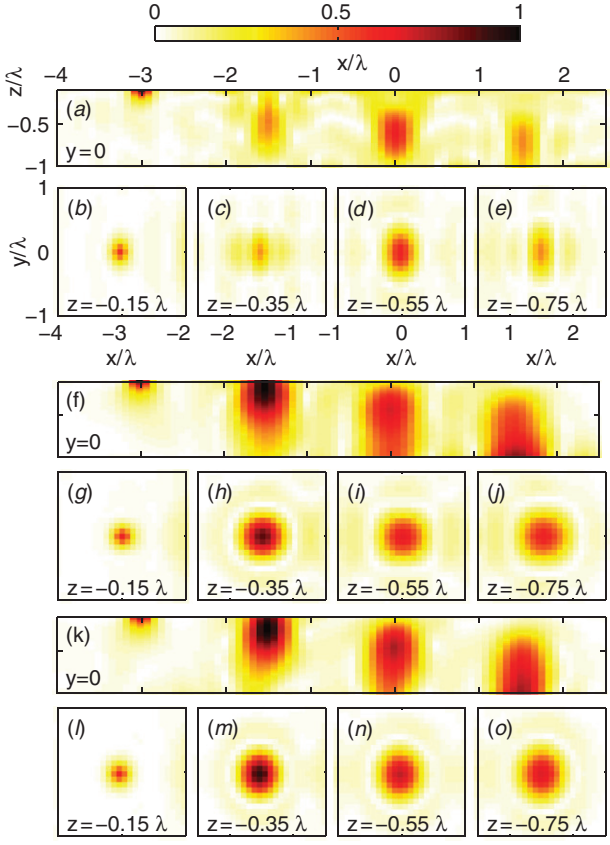

Figure 2. Reconstructions for the many-angle (*a*)–(*e*), single-angle broadband (*f*)–(*j*) and two-angle broadband (*k*)–(*o*) NSOT systems. Plots (*a*), (*f*) and (*k*) show the *x*–*z* plane while the remaining plots give *x*–*y* detail. The axes used for (*a*)–(*e*) are repeated in (*f*)–(*j*) and (*k*)–(*o*). (The color version of this figure is included in the online version of the journal.)

with comparable peak amplitudes. For the purposes of reconstruction, the sample is assumed to lie in the region $-\lambda < z < -0.1\lambda$.

Three NSOT systems are considered: the first is a single wavelength (λ), many-angle system as in [17], with $\boldsymbol{k}$ lying in the *x*–*z* plane and having 32 observation angles evenly spaced across a semicircle; the second system has a single observation angle ($\boldsymbol{k}$ lies in the *x*–*z* plane at 45° from vertical) and 32 observation wavelengths between 0.8λ and 1.2λ; and the third system has the same spectral range as the second but with two observation angles (30° and 60° from vertical in the *x*–*y* plane) and 16 spectral samples per observation angle. All three systems have a scan step of $\lambda/12$ in both *x* and *y*, with 100 and 80 samples in the *x* and *y* directions, respectively.

The synthetic data were inverted according to Equation (15), with N^+ chosen so that any singular components with singular value less than one one-hundredth of the maximum were discarded. This criterion corresponds to a signal-to-noise ratio of approximately 40 dB. The magnitudes of the resulting reconstructions are shown in Figure 2, where each reconstruction (one for each system) has been normalized by its maximum value.

From Figure 2 it can be seen that the resolution for the broadband and limited observation angle NSOT systems is poorer than for the many-angle case at the central frequency of the broadband case, but meaningful three-dimensional detail is given. The resolution in the broadband case may be improved by increasing the bandwidth. However, once full bandwidth is achieved, increasing bandwidth requires increasing central frequency, so the many angle case at the central frequency always gives superior resolution. In all systems the resolution degrades with depth into the sample. Due to asymmetry in the observation angles, the many-angle and two-angle NSOT systems have differing resolutions in the *x* and *y* directions.

7. Discussion

In summary, this work shows how a broadband NSOT system may image three-dimensional structure using a reduced number of observation angles by leveraging the information available in the spectral degree of freedom. Such a system could be achieved through coupling a low-coherence interferometer to a fiber based NSOM system. The advantage of such a system is that it provides a proven means to collect phase sensitive data over a broad band.

It was assumed that the sample is nondispersive, but the results presented can be easily generalized to the case where the sample is characterized by a susceptibility or scattering potential that may be written as the product of a function of only the frequency and a function of only the coordinates, that is, a separable function.

Acknowledgements

This work was supported in part by U.S. Air Force MURI Grant F49620-03-10379. J.C.S. acknowledges support under Grant Nos. NSF DMR 0425780 and USAFOSR FA9550-07-1-0096.

References

[1] Abbe, E. *Arch. Mikroskop. Anatom.* **1873,** *9,* 413–420.
[2] Synge, E.H. *Phil. Mag.* **1928,** *6,* 356–362.
[3] Novotny, L.; Hecht, B. *Principles of Nano-optics*; Cambridge University Press: Cambridge, UK, 2006.

[4] Girard, C.; Dereux, A. *Rep. Progr. Phys.* **1996,** *59,* 657–699.
[5] Ash, E.A.; Nicholls, G. *Nature* **1972,** *237,* 510–512.
[6] Lewis, A.; Isaacson, M.; Harootunian, A.; Muray, A. *Ultramicroscopy* **1984,** *13,* 227–232.
[7] Pohl, D.W.; Denk, W.; Lanz, M. *Appl. Phys. Lett.* **1984,** *44,* 651–653.
[8] Betzig, E.; Trautman, J.K.; Wolfe, R.; Gyorgy, E.M.; Finn, P.L.; Kryder, M.H.; Chang, O.H. *Appl. Phys. Lett.* **1992,** *61,* 142–144.
[9] Carminati, R.; Greffet, J.J. *J. Opt. Soc. Am. A* **1995,** *12,* 2716–2725.
[10] Carminati, R.; Greffet, J.J. *Ultramicroscopy* **1995,** *61,* 11–16.
[11] Carney, P.S.; Frazin, R.A.; Bozhevolnyi, S.I.; Volkov, V.S.; Boltasseva, A.; Schotland, J.C. *Phys. Rev. Lett.* **2004,** *92,* 163903.
[12] Karl, W.C. *Handbook of Image and Video Processing*; Academic: New York, 2000; pp 141–161.
[13] Carney, P.S.; Schotland, J.C. Near-field Tomography. In *Inside Out: Inverse Problems and Applications*: Uhlmann, G.; Series MSRI no. 47; Cambridge University Press, Cambridge, UK, 2003; pp 133–168.
[14] Marks, D.L.; Carney, P.S. *Opt. Lett.* **2005,** *30,* 1870–1872.
[15] Sentenac, A.; Chaumet, P.C.; Belkebir, K. *Phys. Rev. Lett.* **2006,** *97,* 243901.
[16] Gaikovich, K.P. *Phys. Rev. Lett.* **2007,** *98,* 183902.
[17] Carney, P.S.; Schotland, J.C. *Appl. Phys. Lett.* **2000,** *77,* 2798–2800.
[18] Sun, J.; Carney, P.S.; Schotland, J.C. *IEEE J. Sel. Top. Quant.* **2006,** *12,* 1072–1082.
[19] Bao, G.; Li, P. *Opt. Lett.* **2007,** *32,* 1465–1467.
[20] Sun, J.; Carney, P.S.; Schotland, J.C. *J. Appl. Phys.* **2007,** *102,* 103103.
[21] Sun, J.; Schotland, J.C.; Hillenbrand, R.; Carney, P.S. *Appl. Phys. Lett.* **2009,** *95,* 121108.
[22] Schmitt, J.M. *IEEE J. Sel. Top. Quant.* **1999,** *5,* 1205–1215.
[23] Curlander, J.C.; McDonough, R.N. *Synthetic Aperture Radar: Systems and Signal Processing*; Wiley Series in Remote Sensing and Image Processing; Wiley: New York, 1991.
[24] Brehm, M.; Schliesser, A.; Keilmann, F. *Opt. Express* **2006,** *14,* 11222–11233.
[25] Mandel, L.; Wolf, E. *Optical Coherence and Quantum Optics*; Cambridge University Press: Cambridge, UK, 1995; pp 120–125.
[26] Bertero, M.; De Mol, C.; Pike, E.R. *Inverse Problems* **1985,** *1,* 301–330.